The Astrophysical Journal, 932:69 (14pp), 2022 June 10 https://doi.org/10.3847/1538-4357/ac6d5d

Distinct Thermal Emission from GRB 190109A

Rui-Quan Li[1,2], Xiang-Gao Wang[1,2], Lu-Yao Jiang[1,2], Shen-Shi Du[1,2], Hui-Ya Liu[1,2], Ying-Ying Gan[1,2], Zi-Min Zhou[1,2], Da-Bin Lin[1,2], and En-Wei Liang[1,2]
[1] GXU-NAOC Center for Astrophysics and Space Sciences, School of Physical Science and Technology, Guangxi University, Nanning 530004, People's Republic of China; wangxg@gxu.edu.cn
[2] Guangxi Key Laboratory for the Relativistic Astrophysics, Nanning 530004, People's Republic of China
Received 2020 February 19; revised 2022 April 23; accepted 2022 May 4; published 2022 June 16

Abstract

The gamma-ray bursts (GRBs) with distinct thermal components are rarely detected, especially in cases with thermal components throughout the prompt phase. Recently, Fermi/GBM, Swift/BAT, and Swift/XRT detected the special long-duration GRB 190109A, which has four pulses in the prompt gamma-ray emission, i.e, Pulse I (−4 to 20 s), Pulse II (20–50 s), Pulse III (50–90 s), and Pulse IV (90–120 s). GRB 190109A exhibits a very hard low-energy index ($\alpha \sim 1$) in the Band function relative to the typical GRBs ($\alpha \sim -1$). In the whole burst prompt emission, we find distinct thermal emissions in the time-resolved spectra throughout four pulses. The blackbody (BB) temperature kT varies from 24.7 to 8.2 keV for Pulse I to Pulse IV. We also obtain the relation of $F \propto kT^{-0.40}$ for the early phase (Pulse I) and $F \propto kT^{3.33\pm0.76}$ for the late phase (Pulses II–IV), respectively. The significant deviation of the $kT - F$ relation in the early epochs from that in the late epochs likely suggests that the BB spectra origin of the early phase (Pulse I) may have disparate physical processes from those of the late phase (Pulses II–IV). For instance, it may be the transition from cocoon surroundings by a jet to the photosphere of the matter-dominated jet. A jet break is found in the late X-ray afterglow, which is in keeping with the standard external shock afterglow model in the interstellar medium circumburst.

Unified Astronomy Thesaurus concepts: Gamma-ray bursts (629)

1. Introduction

Gamma-ray bursts (GRBs) are the most luminous phenomena observed in the universe (e.g., Kumar & Zhang 2015). The T_{90}-duration time of the GRB prompt phase is defined by Kouveliotou et al. (1993) results in the classification of short (mostly corresponding to type I GRBs; Zhang et al. 2009) and long GRBs (mostly corresponding to type II GRBs; Zhang et al. 2009), with a critical time of 2 s. The long GRBs are deemed to be associated with the core collapse of massive stars (e.g., Narayan et al. 1992; Woosley 1993; MacFadyen & Woosley 1999; Berger et al. 2005; Tanvir et al. 2005; Fruchter et al. 2006; Zhang 2006) and the short GRBs with the mergers of compact binaries, such as the neutron star–neutron star (e.g., Paczynski 1986; Eichler et al. 1989; Abbott et al. 2017) or neutron star–black hole coalescence (e.g., Paczynski 1991).

A massive star collapses into a black hole or magnetar as a central engine, and it powers an ultrarelativistic jet that breaks through the stellar envelope of the progenitor star, which means that a GRB is produced successfully (e.g., Usov 1992; Woosley 1993; Thompson 1994; MacFadyen & Woosley 1999). In some cases, while the GRB jet drives its way through the stellar envelope, its rate of advance is slowed down, and most of the energy output during that period is deposited into a double-shock (forward-reverse) structure that forms at its head (e.g., Ramirez-Ruiz et al. 2002; Matzner 2003; Lazzati & Begelman 2005; Bromberg et al. 2011; Nakar & Piran 2017). The hot head material spills sideways, forming a possible cocoon composed of an outer stellar material and an inner (possibly relativistic) jet (Ramirez-Ruiz et al. 2002; Lazzati & Begelman 2010; Nakar & Piran 2017). This process takes a few seconds (with $R_* \approx 10^{11}$ cm), and the dissipated energy of the jet is significant, indicating that the energy of the hot head material and cocoon gains is comparable to that released by the observed GRBs. If the jet is still opaque at the surface of the stellar envelope, one can thus expect the observable breakout emission component from the cocoon to be released before the jet emission arises. The emission from the cocoon has been proposed as an explanation for the thermal emission of GRBs (Ghisellini et al. 2007; Piro et al. 2014) or for the precursor of GRBs (Lü et al. 2017) and steep decay in the early X-ray afterglow of GRBs (Ramirez-Ruiz et al. 2002; Pe'er et al. 2006; Lazzati et al. 2010). However, these possible signatures of the cocoon emission may be detected, which strongly depends on the physical conditions of mixing between the shocked jet and the shocked stellar cocoon (e.g., Ramirez-Ruiz et al. 2002; Nakar & Piran 2017).

The drastic spectral and temporal variations are observed at prompt emission (e.g., gamma-ray and X-ray bands) and the afterglows (e.g., X-ray, optical, and radio bands; e.g., Mészáros & Rees 1997; Piran 1999), the characteristics of which can be generally explained by a matter or Poynting flux, or a hybrid composition jet model. In terms of a matter-dominated fireball, a quasi-thermal emission from the fireball photosphere and a nonthermal component due to the internal-shock collisions are predicted during the GRB prompt phase (e.g., Mészáros & Rees 2000; Daigne & Mochkovitch 2002; Zhang & Mészáros 2002; Pe'er et al. 2006; Pe'Er et al. 2012; Toma et al. 2011). Moreover, the nonthermal component can be reproduced for a Poynting-flux-dominated fireball, such as the internal-collision-induced magnetic reconnection and turbulence (ICMART) model (Zhang & Yan 2011). The prompt spectra of some bursts, like GRB 110721A, show a subdominant thermal component superposed with a synchrotron

component, indicating a hybrid jet in GRB outflows (Gao & Zhang 2015). Thermal emission (the blackbody (BB) component) is expected to appear in the spectra of the GRBs. Nevertheless, most observational spectra are well fitted by an empirical function of two smoothly connected power laws (PLs), namely, the so-called Band function (Band et al. 1993). Compared to a BB function, this spectrum has a much wider peak and is much softer at low energies. In line with large GRB prompt emission data (e.g., data from Compton/BASTE, Fermi/GBM, Konus-Wind, HETE-2/FREGATE, INTEGRAL/SPI/IBIS, RHESSI, BeppoSAX, Suzaku/WAM, and Swift/BAT), previous studies have shown that some observed low-energy PL indices of the Band component are found to be harder than those predicted by the synchrotron regime of the fast-cooling case ($\alpha = -3/2$) and the slow-cooling case ($\alpha = -2/3$, also called the synchrotron line of death; e.g., Preece et al. 1998; Sari et al. 1998). According to some GRBs, related spectral width is found to be very narrow, suggesting the probable existence of a quasi-thermal component. Besides, it has been observationally confirmed recently, including quasi-thermal component dominant and subdominant GRBs, e.g., GRB 081221 (Hou et al. 2018), GRB 090902B (Ryde et al. 2010; Zhang & Yan 2011), GRB 100507 (Ghirlanda et al. 2013), GRB 100724B (Guiriec et al. 2011), GRB 101219B (Larsson et al. 2015), GRB 110721A (Axelsson et al. 2012; Zhang et al. 2012), GRB 120323A (Guiriec et al. 2013), GRB 141207A (Arimoto et al. 2016), GRB 160625B (Lü et al. 2017; Zhang et al. 2018), and tens of Compton/BATSE GRBs (Ryde 2005; Ryde & Pe'er 2009).

In this paper, we present an analysis of gamma-ray and X-ray emissions from the long GRB 190109A detected by Fermi and Swift. Apart from that, we perform both the time-integrated and time-resolved spectral analysis of the prompt emission concerning GRB 190109A. In the whole burst prompt emission, distinct thermal emissions are found in all the time-resolved spectra throughout four pulses. The data reduction details of Fermi and Swift observations are introduced in Section 2. The analysis of time-integrated and time-resolved spectra, X-ray emission, and results are presented in Section 3. The possible physical interpretations are presented in Section 4. The summaries are presented in Section 5. Throughout the paper, we adopted a concordance cosmology with parameters $H_0 = 71\ \mathrm{km\ s^{-1}\ Mpc^{-1}}$, $\Omega_M = 0.30$, $\Omega_\Lambda = 0.70$, and $F \propto t^{\alpha}\nu^{\beta}$. Moreover, the convention $Q = 10^n Q_n$ is adopted for cgs units.

2. Data Reduction

GRB 190109A was first triggered by Swift/BAT on 2019 January 09 at 05:12:41.78 UT (UT dates are adopted; trigger 882747) with T_{90}=115.0 ± 33.5 s (Gropp et al. 2019). Besides, it was triggered and detected by Fermi/GBM on 2019 January 9 at 05:12:49.45 (denoted as T_0; trigger 568703574/190109217) with T_{90} = 120 s (50–300 keV; von Kienlin 2019) as well. The discrepancy of the detected duration (T_{90}) is caused by the difference in sensitivity of the BAT and GBM energy bands (Qin et al. 2013). The event fluence (10–1000 keV) from Fermi/GBM is $(7.6 \pm 0.6) \times 10^{-6}$ erg cm^{-2}. Apparently, the burst was not detected by the Fermi/LAT instrument. The time-averaged spectrum in this time is fitted by a Band function with $E_p = 46.8 \pm 2.2$ keV, $\alpha = 1.3 \pm 0.3$, and $\beta = -2.71 \pm 0.13$ (von Kienlin 2019). GBM has 12 sodium iodide (NaI) scintillation detectors covering an energy from 8 keV to 1 MeV and two bismuth germanate (BGO) scintillation detectors sensitive to higher energies between 200 keV and 40 MeV (Meegan et al. 2009). Furthermore, we downloaded the Fermi/GBM data of GRB 190109A from the public science support center at the official Fermi website[3] and used our Python code to extract light curves. As is shown in Figure 1, GRB 190109A is a comparatively weak burst with four pulses: Pulse I (−4 to 20 s), Pulse II (20–50 s), Pulse III (50–90 s), and Pulse IV (90–120 s). The BGO is also triggered almost without photons detected. Based on Swift/BAT data and time-tagged event (TTE) data from the $\mathrm{NaI_9}$, $\mathrm{NaI_a}$, and $\mathrm{NaI_b}$ detectors, we perform joint spectral analysis with the Python source packageFermitools,[4] XSPECv12.10.1, heasoft6.25,[5] and the CALDB Version of 2009 August 04.[6]

The X-ray Telescope (XRT) on board Swift began observing the X-ray emission of GRB 190109A from 168.9 to 23823 s after the BAT trigger (Gropp et al. 2019). The XRT data we obtained are from the UK Swift Science Data Center,[7] which is maintained by the XRT team at the University of Leicester. The X-ray light curve of the afterglow is presented in Figure 2. The Ultra-Violet/Optical Telescope (UVOT) on board Swift and the ground-based optical telescopes quickly responded to the optical observations (Gropp et al. 2019; Belkin et al. 2019; Oeda et al. 2019) but failed to detect any optical object within the Swift/XRT position.

3. Data Analysis of GRB 190109A and Results

3.1. Time-integrated Spectrum

Most observational spectra of GRBs are well fitted by an empirical Band function (Band et al. 1993),

$$N_{\mathrm{Band}}(E) = A_1 \begin{cases} \left(\frac{E}{100\ \mathrm{keV}}\right)^{\alpha} \exp\left(-\frac{E}{E_0}\right), & E < (\alpha - \beta)E_0 \\ \left[\frac{(\alpha-\beta)E_0}{100\ \mathrm{keV}}\right]^{\alpha-\beta} \exp(\beta - \alpha)\left(\frac{E}{100\ \mathrm{keV}}\right)^{\beta}, & E \geqslant (\alpha - \beta)E_0, \end{cases} \quad (1)$$

where A_1 represents the normalization of the Band spectrum; α and β are the corresponding low- and high-energy photon spectral indices, respectively; E is the observational photon energy; and E_0 denotes the break energy of the spectrum. Besides, the peak energy (E_p) of the spectrum is related to E_0 through $E_p = (2 + \alpha)E_0$. We first fit the time-integrated spectrum data for the joint Swift/BAT and Fermi/GBM in −4 to 120 s with a Band function. The best-fitting parameters of the Band function model are $\alpha = 0.93 \pm 0.39$, $\beta = -2.61 \pm 0.15$, and $E_p = 45.1 \pm 10.3$ keV with PGSTAT/dof = 351/411. The time-integrated spectral parameters in the Band function model by the Fermi/GBM data are $\alpha = 1.44 \pm 0.66$, $\beta = -2.47 \pm 0.18$, and $E_p = 43.4 \pm 14.6$ keV, which is consistent with the results of von Kienlin (2019). We also fit the Swift/BAT time-integrated spectra with a Band function and got the parameters $\alpha = 0.35 \pm 0.62$, $\beta =$

[3] http://legacy.gsfc.nasa.gov/Fermi/data/
[4] http://fermi.gsfc.nasa.gov/ssc/data/analysis/software/
[5] https://heasarc.gsfc.nasa.gov/docs/software/lheasoft/download.html/
[6] https://heasarc.gsfc.nasa.gov/docs/heasarc/caldb/
[7] https://www.swift.ac.uk/burst-analyser/00882747/

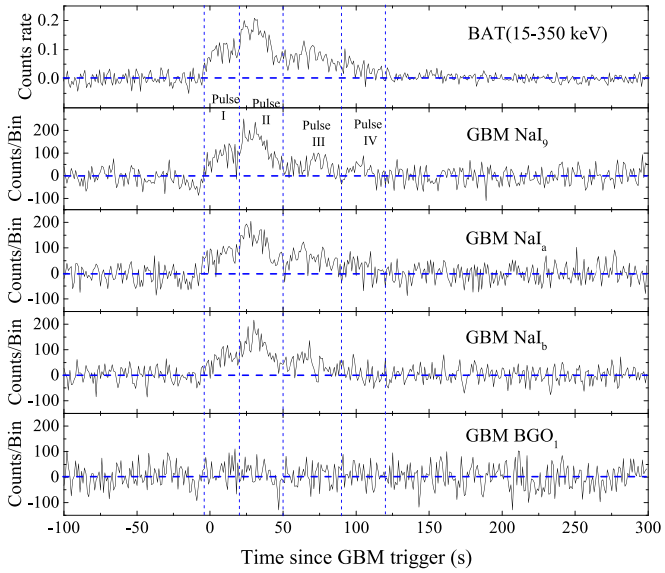

Figure 1. GBM and BAT light curves for the gamma-ray emission of GRB 190109A with a bin size of 1 s. The whole burst could be divided into four pulses by dashed lines: Pulse I (−4 to 20 s), Pulse II (20–50 s), Pulse III (50–90 s), and Pulse IV (90–120 s).

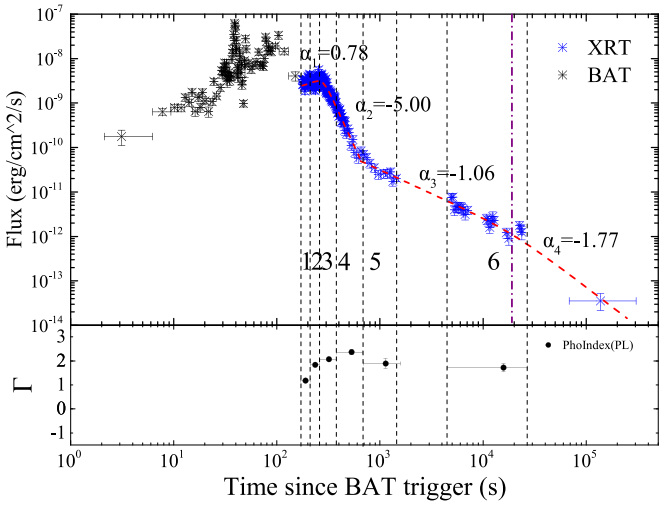

Figure 2. The top panel shows Swift/BAT data converted to 0.3−10 keV and Swift/XRT light curves of GRB 190109A. The jet break times are shown by the purple vertical dashed–dotted line. The vertical black dashed lines mark the time slices we divided. The inset of the bottom panel shows the photon index of each time slice.

-2.54 ± 0.25, and $E_p = 46.1 \pm 20.0$ keV. The fitting results are shown in Table 1 and Figure 3.

Note that Gropp et al. (2019) reported that the Swift/BAT can be fitted by a cutoff PL (CPL) function, with $\alpha = -0.36 \pm 0.47$, $E_p = 49.7 \pm 4.0$, and PGSTAT/dof = 46/56. We also employed the CPL function to fit the GRB 190109A. The CPL function can be written as

$$N_{\rm CPL}(E) = A_2 \left(\frac{E}{100\ {\rm keV}}\right)^{\alpha} \exp\left(-\frac{E}{E_c}\right), \quad (2)$$

where A_2 represents the normalization of the CPL spectrum and E_c is the cutoff energy, similar to the E_0 of the Band function. The results of fitting the Swift/BAT are consistent with the results of Gropp et al. (2019), with $\alpha = -0.35 \pm 0.26$, $E_p = 52.7 \pm 12.8$, and PGSTAT/dof = 51/55. The results of joint fitting Swift/BAT and Fermi/GBM with CPL are $\alpha = -0.04 \pm 0.17$, $E_p = 54.7 \pm 7.3$, and PGSTAT/dof = 367/412 (as shown in Table 1). We also calculate the BIC[8] for the Band and CPL model, respectively. We found that $\Delta{\rm BIC} = {\rm BIC_{CPL}} - {\rm BIC_{Band}} = 385 - 375 = 10$, which may indicate that the Band model is preferred. However, the statistics in the GBM data are not really good enough to constrain the best-fit spectral model. Furthermore, if a detector's energy band is not wide enough, or the detector has a low statistics of the high-energy photon counts, the high-energy photon index β of the Band function will not be well constrained, and the spectrum of the GRB sometimes can be fitted by a CPL function. Most GRBs with CPL may have an intrinsic Band spectrum whose high-energy spectral index is not well constrained .

To investigate the spectral properties more, we fit the spectra that only selected the data of 8–70 keV for Fermi/GBM and 15–70 keV for Swift/BAT, respectively. As shown in Table 1, the value of α is harder than the previous one, with 0.37 ± 0.47 and 1.29 ± 0.49 for Swift/BAT (15–70 keV) and Fermi/GBM (8–70 keV), respectively. The α values are similar to the Band model in the whole energy one. For the joint spectra of Swift/BAT (15–70 keV) and Fermi/GBM (8–70 keV), we can get the hard α value ($\alpha = 0.92 \pm 0.31$), which is also similar to the α of the Band model in the whole energy band ($\alpha = 0.93 \pm 0.39$). As shown in Table 1 and Figure 3, the value of the low-energy photon spectral index α for both the CPL and Band functions in the range of 8/15–70 keV is $\alpha \sim 1$, which are consistent with the whole Swift-Fermi time-integrated spectrum with a Band function. Our results show that the α of GRB 190109A is significantly hard ($\alpha \sim 1$). Concerning the physical origin of the Band function, it is interpreted as the synchrotron emission of the Poynting-flux-dominated outflow (Uhm & Zhang 2014; Zhang et al. 2016). The median value of α for long GRBs is ~ -1 (e.g, Preece et al. 2000; Nava et al. 2011; Zhang & Yan 2011), and the Band function low-energy PL index of GRB 190109A is harder than the synchrotron line of death ($\alpha = -2/3$). Such a spectrum signifies a significant contribution of thermal emission from the fireball photosphere (e.g., Mészáros & Rees 2000; Ryde et al. 2010). Hence, it is essential to introduce other models (e.g., the BB component) to interpret the data of GRB 190109A.

A single BB is invoked to describe the fireball photosphere emission (Rees & Mészáros 2005; Pe'er et al. 2006; Giannios 2008; Beloborodov 2010). If it is in the Rayleigh–Jeans regime, the index for a BB is $\alpha \sim 1$. We attempt to fit the time-integrated spectrum data with a single BB model, which is

[8] Since the number of free parameters differs in models, we employ the Bayesian information criterion (BIC; Kass & Raftery 1995) to evaluate the goodness between them. BIC is a criterion for model selection among a finite set of models, which can be written as BIC $= -2lnL + k \cdot ln(n)$, where L is the maximum likelihood value, k is the number of fitted parameters, and n is the number of data points. We define $\Delta{\rm BIC} = {\rm BIC_1} - {\rm BIC_2}$, where ${\rm BIC}_i$ corresponds to Model i ($i = 1, 2$). The model with the lowest BIC is preferred, and its significance level could be calculated with ΔBIC (Trotta 2008): (1) if $0 < \Delta{\rm BIC} < 2$, the preference for Model 2 is not worth more than a bare mention, with the significance level being less than 2.1σ; (2) if $2 < \Delta{\rm BIC} < 6$, the preference for Model 2 is positive, with the significance level being $2.1\sigma - 3.0\sigma$; (3) if $6 < \Delta{\rm BIC} < 10$, the preference for Model 2 is strong, with the significance level being $3.0\sigma - 3.6\sigma$; (4) if $10 < \Delta{\rm BIC}$, the preference for Model 2 is very strong, with the significance level being $> 3.6\sigma$.

Table 1
The Spectral Fitting with CPL and Band Model

Time Interval	Detector	CPL[a]		PGSTAT/dof	CPL(8(15) −70 keV)[b]		PGSTAT/dof	Band[a]			PGSTAT/dof
(s)		α	E_p(keV)		α	E_p(keV)		α	β	E_p(keV)	
Entire: −4.0 to 120.0	BAT	-0.35 ± 0.26	52.7 ± 12.8	51/55	0.37 ± 0.47	46.8 ± 14.6	23/22	0.35 ± 0.62	-2.54 ± 0.25	46.1 ± 20.0	45/54
	GBM	0.11 ± 0.24	58.8 ± 11.4	306/354	1.29 ± 0.49	44.7 ± 11.3	56/104	1.44 ± 0.66	-2.47 ± 0.18	43.4 ± 14.6	300/353
	GBM-BAT	-0.04 ± 0.17	54.7 ± 7.3	367/412	0.92 ± 0.31	45.5 ± 7.8	83/129	0.93 ± 0.39	-2.61 ± 0.15	45.1 ± 10.3	351/411
Pulse I: −4.0 to 20.0	BAT	-0.48 ± 0.40	101.8 ± 60.7	48/55	1.33 ± 1.03	55.1 ± 28.8	19/22	1.41 ± 1.91	-1.70 ± 0.24	52.9 ± 55.8	43/54
	GBM	0.49 ± 0.30	87.9 ± 18.5	359/354	...	...	...	0.83 ± 0.46	-2.87 ± 0.56	78.8 ± 25.7	358/353
	GBM-BAT	0.18 ± 0.23	89.2 ± 16.9	367/412	...	...	...	1.05 ± 0.55	-2.31 ± 0.21	67.4 ± 22.7	410/411
−4.0 to 10.0	BAT	-0.08 ± 0.59	117.0 ± 77.5	43/55	0.90 ± 1.52	69.2 ± 68.6	16/22	1.17 ± 2.82	-1.34 ± 0.29	62.3 ± 114.9	43/54
	GBM	1.04 ± 0.48	105.6 ± 29.0	392/354	...	...	...	0.99 ± 0.48	−8.81(fixed)	108.8 ± 30.1	392/353
	GBM-BAT	0.61 ± 0.33	106.2 ± 25.5	440/412	...	...	...	0.73 ± 0.36	−7.94(fixed)	105.7 ± 25.2	441/411
10.0−20.0	BAT	-0.15 ± 0.66	62.4 ± 36.7	62/55	1.99 ± 1.37	46.7 ± 25.1	19/22	1.98 ± 2.22	-2.38 ± 0.48	46.1 ± 43.3	56/54
	GBM	1.26 ± 0.52	56.2 ± 14.5	334/354	...	...	...	1.73 ± 0.83	-3.49 ± 0.82	52.9 ± 20.1	331/353
	GBM-BAT	0.88 ± 0.41	56.6 ± 13.2	399/412	...	...	...	2.01 ± 0.91	-2.84 ± 0.36	48.5 ± 18.7	391/411
Pulse II: 20.0−50.0	BAT	0.13 ± 0.34	52.5 ± 12.9	59/55	0.61 ± 0.56	49.5 ± 17.2	19/22	0.68 ± 0.65	-2.78 ± 0.39	48.0 ± 19.3	54/54
	GBM	0.54 ± 0.20	54.3 ± 6.9	371/354	...	...	...	0.78 ± 0.28	-3.68 ± 0.55	51.8 ± 8.7	370/353
	GBM-BAT	0.25 ± 0.16	54.0 ± 6.4	448/412	...	...	...	0.67 ± 0.25	-3.25 ± 0.32	50.1 ± 7.8	443/411
20.0−30.0	BAT	0.48 ± 0.45	58.7 ± 17.2	59/55	1.21 ± 0.82	53.5 ± 22.7	25/22	0.84 ± 0.73	-2.95 ± 0.78	55.4 ± 24.2	58/54
	GBM	0.65 ± 0.26	61.3 ± 9.8	408/354	...	...	...	0.58 ± 0.26	−9.37(fixed)	62.1 ± 10.2	308/353
	GBM-BAT	0.53 ± 0.22	60.6 ± 8.8	474/412	...	...	...	0.53 ± 0.22	−9.37(fixed)	60.6 ± 8.8	474/411
30.0−40.0	BAT	-0.22 ± 0.46	55.6 ± 22.7	63/55	0.54 ± 0.82	48.8 ± 25.4	26/22	1.29 ± 1.52	-2.34 ± 0.30	42.9 ± 33.4	57/54
	GBM	0.54 ± 0.27	53.0 ± 9.0	366/354	...	...	...	0.75 ± 0.35	-4.13 ± 1.05	51.1 ± 10.5	366/353
	GBM-BAT	0.24 ± 0.23	53.3 ± 8.4	441/412	...	...	...	0.62 ± 0.34	-3.33 ± 0.48	49.7 ± 10.8	440/411
40.0−50.0	BAT	0.21 ± 0.93	40.7 ± 24.8	45/55	-0.07 ± 1.17	42.5 ± 40.1	14/22	0.34 ± 0.98	-9.37 ± 0.79	40.9 ± 25.2	45/54
	GBM	1.26 ± 0.73	39.7 ± 8.4	360/354	...	...	...	1.33 ± 0.72	−9.37(fixed)	39.6 ± 13.3	359/353
	GBM-BAT	1.02 ± 0.54	40.0 ± 11.1	404/412	...	...	...	0.70 ± 0.51	−9.31(fixed)	41.0 ± 11.8	406/411
Pulse III: 50.0−90.0	BAT	-0.62 ± 0.50	43.5 ± 23.4	52/55	-0.78 ± 0.74	43.8 ± 41.6	24/22	-0.76 ± 0.56	-3.62 ± 5.10	43.8 ± 29.6	52/54
	GBM	0.12 ± 0.42	46.0 ± 13.9	300/354	...	...	...	1.07 ± 0.83	-2.89 ± 0.40	38.3 ± 17.5	297/353
	GBM-BAT	0.12 ± 0.32	44.8 ± 10.1	354/412	...	...	...	0.60 ± 0.56	-2.94 ± 0.37	40.3 ± 14.4	352/411
50.0−70.0	BAT	-0.08 ± 0.75	40.9 ± 23.1	48/55	-0.04 ± 1.02	42.1 ± 33.6	29/22	-0.68 ± 0.76	-3.89 ± 8.79	41.3 ± 34.6	49/54
	GBM	0.42 ± 0.53	43.7 ± 14.6	318/354	...	...	...	1.14 ± 0.88	-3.26 ± 0.73	39.3 ± 18.6	317/353
	GBM-BAT	0.43 ± 0.42	42.3 ± 11.2	367/412	...	...	...	0.94 ± 0.67	-3.28 ± 0.59	39.3 ± 14.4	366/411
70.0−90.0	BAT	-1.13 ± 0.63	47.6 ± 50.8	50/55	-1.03 ± 1.07	41.7 ± 71.0	19/22	-1.03 ± 0.77	-3.19 ± 6.12	47.4 ± 58.0	50/54
	GBM	-0.11 ± 0.57	46.7 ± 22.7	333/354	...	...	...	-0.21 ± 0.55	−9.37(fixed)	48.6 ± 24.3	333/353
	GBM-BAT	-0.23 ± 0.41	47.8 ± 17.6	388/412	...	...	...	-0.24 ± 0.41	−9.37(fixed)	48.1 ± 17.6	388/411

Table 1
(Continued)

Time Interval	Detector		CPL[a]	PGSTAT/dof		CPL(8(15) −70 keV)[b]	PGSTAT/dof		Band[a]		PGSTAT/dof
	BAT	-0.72 ± 1.42	25.6 ± 36.0	57/55	-0.93 ± 1.63	25.1 ± 48.6	21/22	-0.40 ± 1.50	-9.37 ± 6.14	27.7 ± 33.9	50/54
Pulse IV: 90.0−120.0	GBM	0.65 ± 1.25	33.5 ± 25.8	385/354	...	...	...	0.41 ± 1.23	−9.27(fixed)	34.8 ± 27.1	385/353
	GBM-BAT	1.87 ± 1.16	31.7 ± 13.8	440/412	...	...	...	0.32 ± 0.86	−8.89(fixed)	32.8 ± 17.7	444/411

Notes.
[a] Selected 8−900 keV for Fermi/GBM and 15–150 keV for Swift/BAT.
[b] Only selected 8−70 keV for Fermi/GBM and 15–70 keV for Swift/BAT.

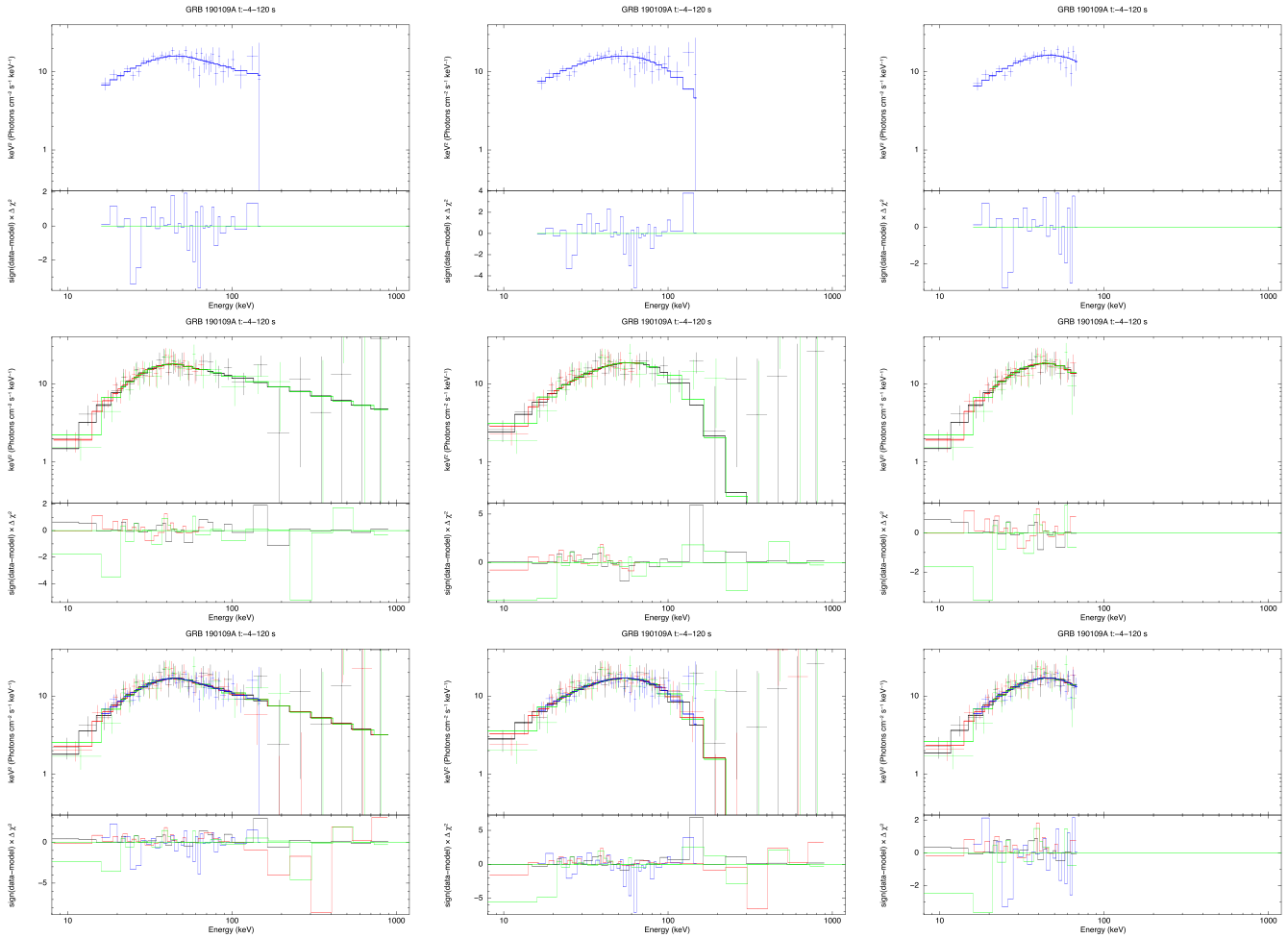

Figure 3. The fitting results of time-integrated spectra of GRB 190109A prompt emission with the Band (left column) and CPL (middle and right columns) functions. For the right column, only the data of 15–70 keV for Swift/BAT and 8–70 keV for Fermi/GBM are selected to model fitting. Spectra from Swift/BAT, Fermi/GBM, and Swift-Fermi data are presented in the top, middle, and bottom rows, respectively. The NaI_9, NaI_a, NaI_b, and BAT data are represented by black, red, green, and blue dots, respectively.

listed as follows:

$$N_{\rm BB}(E) = A_3 \frac{E^2}{\exp(E/kT) - 1}, \quad (3)$$

where A_3 is the normalization of the BB spectrum and kT is the BB temperature. The BB model best-fitting parameters are $kT = 12.5 \pm 0.2$ keV and PGSTAT/dof = 423/413.

It is worth noting that usually there is a PL tail that extends from the peak of thermal radiation, e.g., GRB 090902B (Ryde et al. 2010). Also, we attempt to fit the time-integrated spectrum data with the BB model plus a PL function, written as

$$N_{\rm BB+PL}(E) = A_4 \frac{E^2}{\exp(E/kT) - 1} + A_5 \cdot E^{\Gamma_{\rm PL}}, \quad (4)$$

where A_4 and A_5 are the normalizations of the BB and PL spectrum, respectively; $\Gamma_{\rm PL}$ denotes the single PL photon index. We found that the BB+PL model best-fitting parameters are $kT = 12.0 \pm 0.4$ keV and $\Gamma = -1.56 \pm 0.12$, with PGSTAT/dof = 368/411. The BIC is employed to evaluate the goodness between BB and BB+PL. As shown in Table 2 and Figure 4, the results show that the BB+PL is preferred, with $\Delta{\rm BIC}_{\rm BB+PL-BB} = -43$ (as shown in Table 2).

Since the light curve of GRB 190109A prompt emission consists of four pulses, we also carry out spectral analysis for each pulse separately, with the relevant results presented in Table 2 and Figure 5. With respect to the Band function, the α value for Pulses I–IV is 1.05 ± 0.55, 0.67 ± 0.25, 0.60 ± 0.56, and 0.32 ± 0.86, respectively. As shown in Table 1, the results from the fitting with CPL also suggest that the α value of GRB 190109A for Pulses I–IV is still significantly hard too. For the BB model, the temperature kT values of the BB are 19.1 ± 0.6 keV, 13.8 ± 0.6 keV, 10.2 ± 0.5 keV, and 8.2 ± 0.6 keV, respectively. In regard to the BB+PL model, the kT values are 18.8 ± 1.1 keV, 13.6 ± 0.8 keV, 10.1 ± 0.5 keV, and 8.0 ± 0.7 keV for Pulses I–IV, respectively.

Comparing the goodness of BB spectrum fitting with BB +PL fitting, we get BIC results that the BB+PL model somehow is more preferred in the first three pulses, as shown in Table 2. For the BB+PL model, it is noteworthy that there is a PL tail that extends from the thermal radiation to the higher-energy zone. The inverse Compton scattering may produce a PL tail extending from the peak of the thermal radiation, at

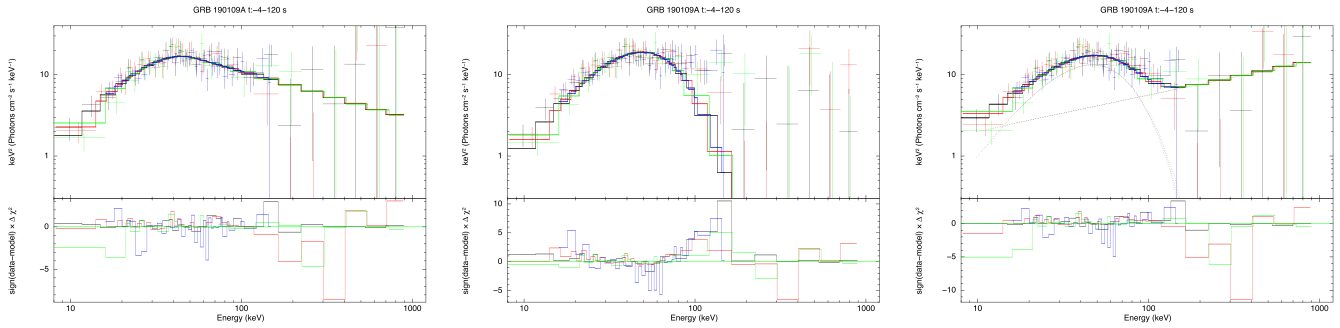

Figure 4. Comparison the fitting result of the time-integrated spectrum of GRB 190109A prompt emission with the Band function (left panel), BB model (middle panel), and BB+PL model (right panel). The NaI_9, NaI_a, NaI_b, and BAT data are represented by black, red, green, and blue dots, respectively.

Table 2
The Joint Spectral Fits of GRB 190109A Using the Fermi/GBM and Swift/BAT Data with the BB and BB+PL Models

Time Interval (s)	BB kT (keV)	PGSTAT/dof	BIC_{BB}	BB+PL kT (keV)	Γ	PGSTAT/dof	BIC_{BB+PL}	ΔBIC[a]	BIC-selected Model Significance Level
Entire:−4.0 to 120.0	12.5 ± 0.2	423/413	435	12.0 ± 0.4	-1.56 ± 0.12	368/411	392	−43	BB+PL($> 5.0\sigma$)
Pulse I:−4.0 to 20.0	19.1 ± 0.6	436/413	448	18.8 ± 1.1	-1.35 ± 0.19	421/411	445	−3	BB+PL(2.3σ)
−4.0 to 10.0	24.7 ± 1.1	445/413	457	25.2 ± 1.6	-1.63 ± 1.30	445/411	469	12	BB(3.9σ)
10.0−20.0	13.8 ± 0.6	401/413	413	13.6 ± 0.8	-1.39 ± 0.61	399/412	423	10	BB(3.7σ)
Pulse II: 20.0−50.0	12.7 ± 0.2	484/413	496	12.7 ± 0.4	-1.68 ± 0.16	457/411	481	−15	BB+PL(4.3σ)
20.0−30.0	14.5 ± 0.4	490/413	502	14.7 ± 0.6	-1.75 ± 0.35	483/409	507	5	BB(2.7σ)
30.0−40.0	12.4 ± 0.3	462/413	474	13.0 ± 0.6	-1.93 ± 0.25	446/411	470	−4	BB+PL(2.5σ)
40.0−50.0	10.2 ± 0.5	406/413	418	10.1 ± 0.5	−1.67(fixed)	407/413	431	13	BB(4.1σ)
Pulse III: 50.0−90.0	10.6 ± 0.4	370/413	382	10.6 ± 0.7	-1.79 ± 0.24	357/411	381	−1	BB+PL(1.7σ)
50.0−70.0	10.3 ± 0.4	372/413	384	10.4 ± 0.7	-1.86 ± 0.43	367/411	391	7	BB(3.1σ)
70.0−90.0	10.7 ± 0.5	400/413	412	11.2 ± 1.1	-1.91 ± 0.40	394/411	418	6	BB(3.0σ)
Pulse IV: 90.0−120.0	8.2 ± 0.6	440/413	453	8.0 ± 0.7	−1.7(fixed)	444/413	468	15	BB(4.3σ)

Note.
[a] The ΔBIC is the value of $BIC_{BB+PL-BB}$.

several hundred keV, to several tens of MeV, and possibly up to GeV energies (e.g., Lazzati & Begelman 2010).

3.2. Time-resolved Spectrum

To get more details on the prompt emission of GRB 190109A, we divided the first three pulses (Pulses I−III) into seven slices (not including Pulse IV, due to not being bright enough and low statistics high-energy photon counts). We fit the time-resolved spectra with the CPL, the Band function, the BB model, and the BB+PL model. The fitting results are shown in Tables 1 and 2 and Figure 6. The fitting results show that α values of low-energy photon spectral indices from the Band function or CPL model in all time-resolved spectra are extremely hard, far beyond the synchrotron line of death ($\alpha = -2/3$). Thus, we suggest thermal emissions in the time-resolved spectrum of GRB190109A, which also leads to the time-integrated spectrum with a hard low-energy index. Comparing the edges of the BB spectrum fitting with that of BB+PL fitting based on the BIC, the results show that the BB model is preferred, with 4/8 very strong slices ($\Delta BIC_{BB+PL-BB} > 10$) and 3/8 positive/strong slices ($2 < \Delta BIC_{BB+PL-BB} < 10$). Only 1/8 slice shows that the BB+PL model is positive and the significance of the PL component with 2.5σ. Also, we note that the statistics in the GBM data are not good enough to constrain the best-fit spectral model between BB and BB+PL. However, the results further illustrate that the thermal component dominates in the prompt emission phase.

3.3. Parameter Correlation in the Prompt Emission

For the energy range from 8 keV to 1 MeV, we acquire the energy flux (erg cm^{-2} s^{-1}) via integrating the F_E (erg cm^{-2} s^{-1} keV^{-1}) spectrum of the BB model. Figure 7 shows that the correlation of kT and energy flux F can be well fitted by a broken PL function with the slope $\alpha_{kT-F,1} = 3.33 \pm 0.76$ and $\alpha_{kT-F,2} = -0.40$. For Pulses II–IV (20–120 s), it is well described by a positive-monotonic relation $F \propto kT^{\alpha_{kT-F,1}} = kT^{3.33 \pm 0.76}$. For Pulse I (−4 to 20 s), it significantly deviates from the relationship of Pulses II–IV, with $F \propto kT^{\alpha_{kT-F,2}} = kT^{-0.40}$.

Ito et al. (2019) suggested that the *Yonetoku* relation, namely, the relation between spectral peak energy E_p and peak luminosity, is the tightest correlation found in the properties of the prompt phase of GRB emission, providing the best diagnostic for the radiation mechanism. Results of GRB 190109A (Figure 8), with a range from $z \sim 0.7$ to 8 (noting that the redshift of GRB 190109A is unknown), are plotted with the observational data of 101 GRBs (Yonetoku et al. 2010) and photospheric emission simulation results (Ito et al. 2019). The $E_p - L_{\gamma,iso}$ relation for the time-resolved spectra of GRB 190109A in accord with that for the time-integrated spectra of the Yonetoku sample (101 bursts;

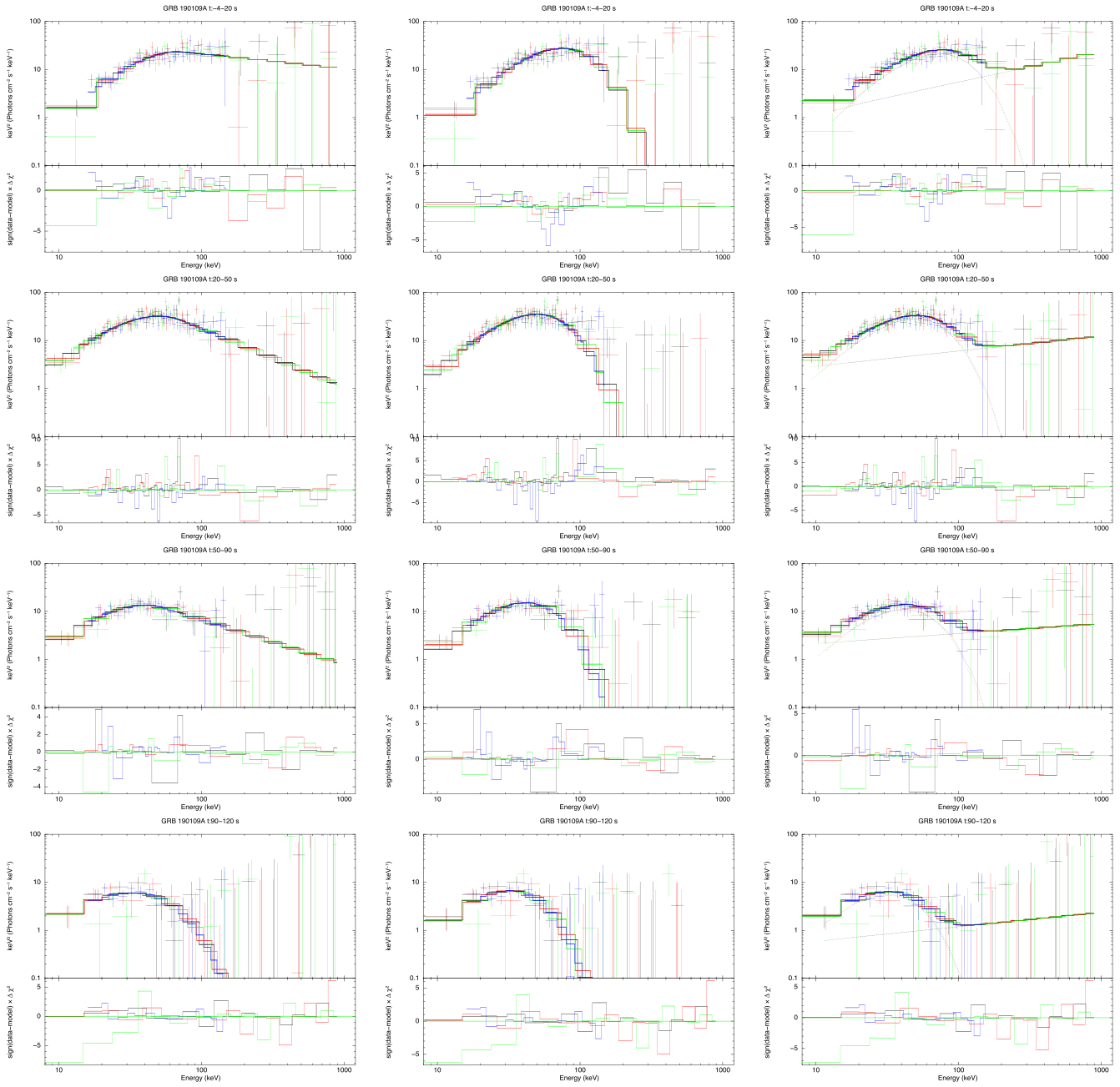

Figure 5. Comparison the fitting results of four pulses' (Pulses I–IV) spectra of GRB 190109A prompt emission with the Band function (left column), BB model (middle column), and BB+PL model (right column). From top row to bottom row is Pulse I to Pulse IV. The selected time slice is also marked on each spectrum. The NaI_9, NaI_a, NaI_b, and BAT data are represented by black, red, green, and blue dots, respectively.

Yonetoku et al. 2010) and photospheric emission simulation results (Ito et al. 2019).

3.4. X-ray Afterglow

To get the temporal profile of the GRB 190109A X-ray afterglow, we fit the light curve with a broken PL function,

$$F(t) = F_0\left[\left(\frac{t}{t_b}\right)^{\omega\alpha_1} + \left(\frac{t}{t_b}\right)^{\omega\alpha_2}\right]^{-1/\omega}, \quad (5)$$

where α_1 and α_2 are the decay indices before and after the break, respectively; t_b is the break time; and ω represents the sharpness of the break. In our fitting, the sharpness parameter ω is adopted as 3. As shown in Figure 2, it seems that the prompt emission still present in the initial phase of X-ray emission (Phase I), with a rising slope of $\alpha_1 = 0.78 \pm 0.25$. After reaching the peak at 280 ± 5.4 s, it then decays with a slope of $\alpha_2 = -5.0 \pm 0.19$ (Phase II). Subsequently, the flux performs normal decay (Phase III) with $\alpha_3 = -1.06 \pm 0.03$ and then transits to a post-jet break (Phase IV) with $\alpha_4 = -1.77 \pm 0.2$.

To investigate the spectral properties of the X-ray time, time-resolved spectra of the X-ray emission in the energy range 0.3–10 keV were extracted for six slices (Figure 9). Besides, XSPECv12.10.1, heasoft6.25,[9] and the CALDB Version of 2009 August 04[10] were employed for the spectral analysis. The

[9] https://heasarc.gsfc.nasa.gov/docs/software/lheasoft/download.html/
[10] https://heasarc.gsfc.nasa.gov/docs/heasarc/caldb/

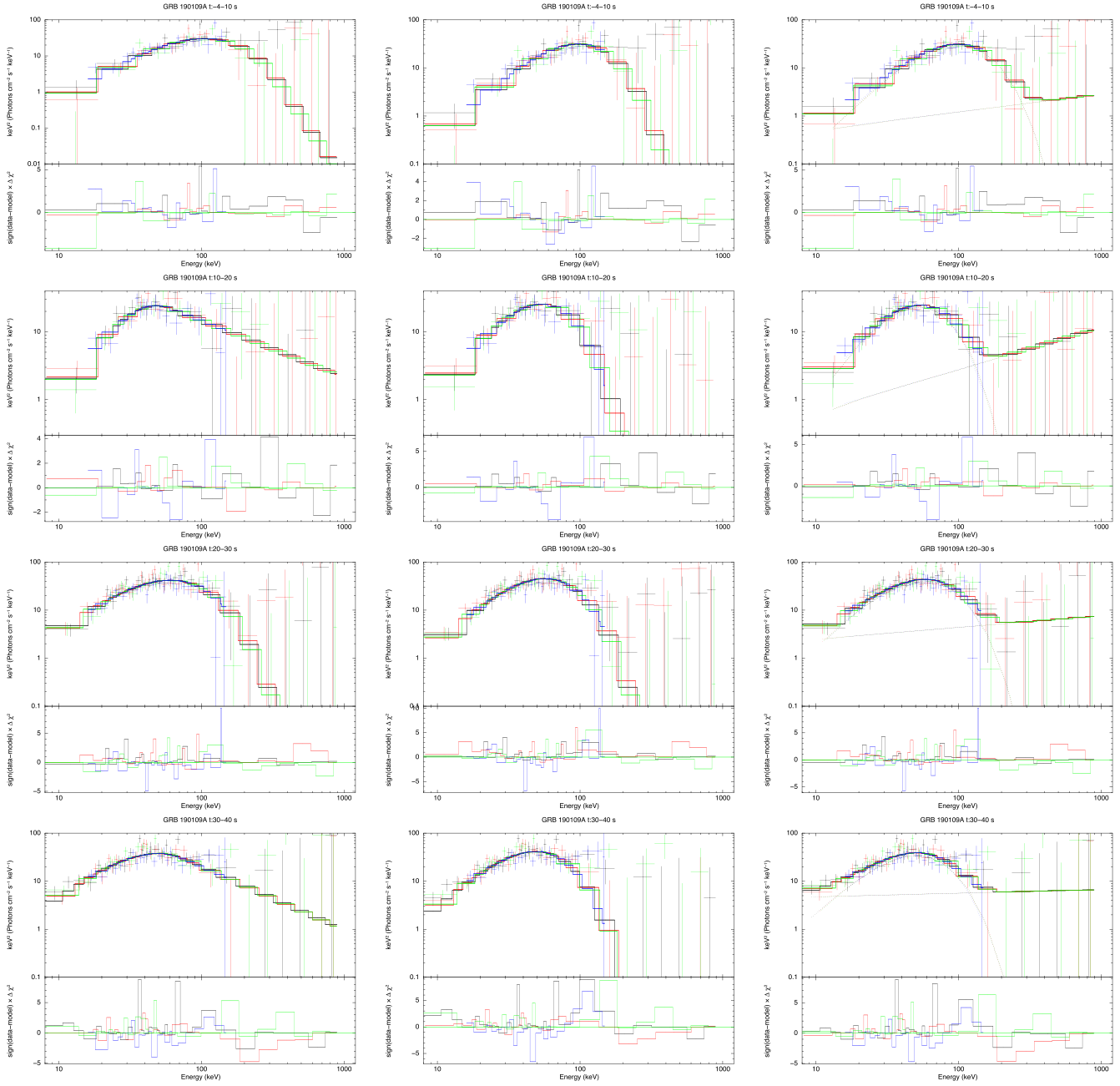

Figure 6. Comparison of the fitting result of time-resolved spectra of GRB 190109A prompt emission with the Band function (left column), BB model (middle column), and BB+PL model (right column). The time interval is also marked on each spectrum. The NaI_9, NaI_a, NaI_b, and BAT data are represented by black, red, green, and blue dots, respectively.

XRT data are corrected for the photoelectric absorption of hydrogen in our Galaxy and the host galaxy, with the equivalent hydrogen column density of our Galaxy being $N_{\rm H} = 4.25 \times 10^{20}\,{\rm cm}^{-2}$. The line-of-sight value of $N_{\rm H}$ in the host galaxy is $\sim 1.0 \times 10^{22}$ cm^{-2}, derived from the time-integrated X-ray afterglow spectrum and fixed at this value in our time-resolved spectral fits. The narrow Slice 1 (175−210 s) shows a hard spectrum with a photon index $\Gamma = -1.18 \pm 0.06$, which is softer than the low-energy value of the Plank function of thermal (narrow) spectra and harder than the dead line of synchrotron emission. It may imply that the X-ray band of prompt emission originates from the superposition of the diminished photosphere emission and a nonthermal component of forming internal shocks. Slices 2 (210−260 s), 3 (260−380 s), and 4 (380−682 s) reveal softer spectra, with $\Gamma = -1.84 \pm 0.13$, $\Gamma = -2.07 \pm 0.04$, and $\Gamma = -2.37 \pm 0.11$. For the afterglow phase (Slices 5 (682−1593 s) and 6 (4500−27,000 s)), the photon index is $\Gamma = -1.90 \pm 0.19$ and $\Gamma = -1.72 \pm 0.16$, respectively. There we adopted an average spectral index $\beta = -0.76 \pm 0.17$ (an average photon index $\Gamma = -1.76 \pm 0.17$, $\beta = \Gamma + 1$). Phases III and IV in the X-ray emission are in keeping with the *closure−relation* of an afterglow model (more details are provided by Zhang et al. 2006; Gao et al. 2013; Wang et al. 2015) in the circumburst medium interstellar medium (ISM), with Phase III (normal decay, pre-jet break)

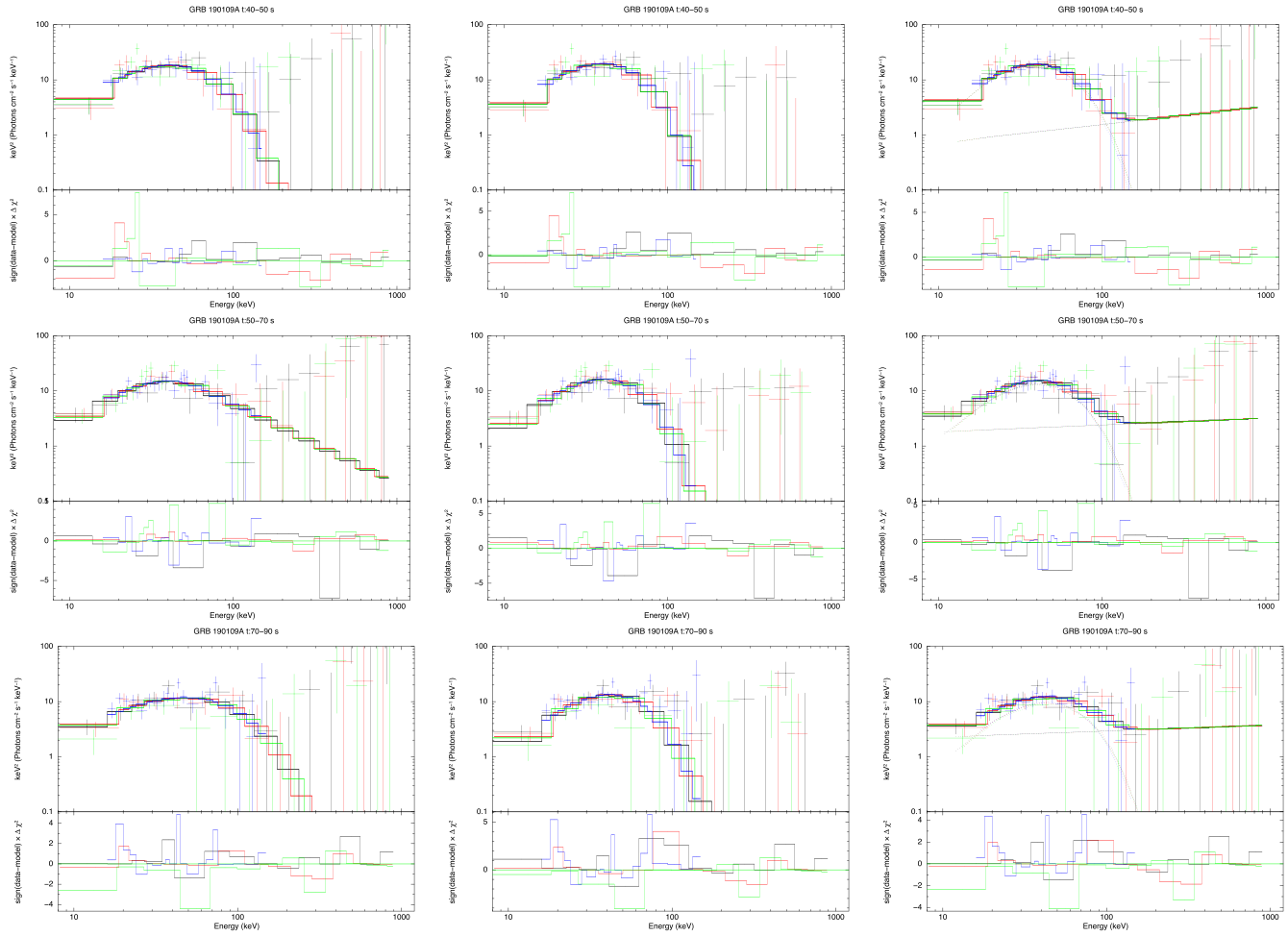

Figure 6. (Continued.)

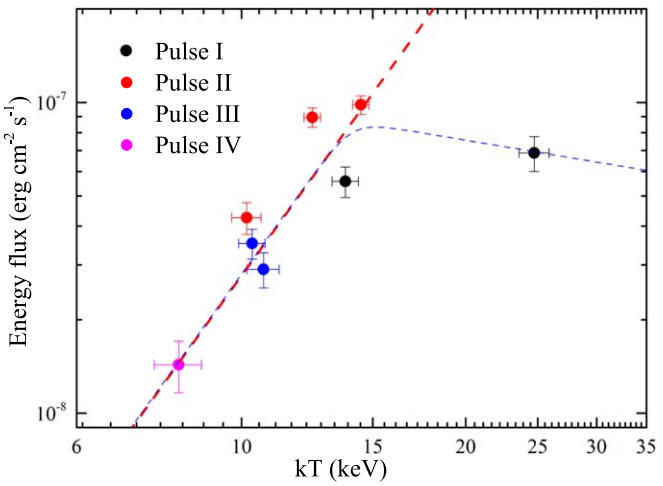

Figure 7. Temperature vs. energy flux of the BB. The data of Pulses I–IV are marked with black, red, blue, and orange dots, respectively. It can be well described with a broken PL function, with $F \propto kT^{-0.40}$ and $F \propto kT^{3.33\pm0.76}$ for early phase (Pulse I) and late phase (Pulses II–IV), respectively.

$\alpha = 3\beta/2 = 3/2 \times 0.76 = 1.14 \backsimeq \alpha_3$ and Phase IV (post-jet break) $\alpha = 3\beta/2 + 0.75 = 3/2 \times 0.76 + 0.75 = 1.89 \backsimeq \alpha_4$. The fitting results are shown in Table 3 and Figure 9. Furthermore, the late X-ray afterglows are consistent with the standard external shock model.

4. Possible Physical Implications and Discussion

4.1. Prompt Emission: Transition from Cocoon (Pulse I) to Fireball Photosphere (Pulses II–IV)?

As is mentioned in Section 2, a very small portion of GRBs are reported to show an extremely narrow energy spectrum and α exceeding the synchrotron limit, signifying that thermal emission is dominated. They can be fitted well with a BB or BB +PL model, e.g., GRB 090902B (Ryde et al. 2010; Zhang & Yan 2011), GRB 101219B (Larsson et al. 2015), and GRB 160625B (the first pulse in the prompt emission; Zhang et al. 2018). For some cases, considering that time-integrated spectra may derive from the contributions of various BB radiation, a multicolor BB (mBB) model, such as GRB 081221 (Hou et al. 2018), GRB 090902B (Ryde et al. 2010; Zhang & Yan 2011), GRB 100507 (Ghirlanda et al. 2013), and GRB 160625B (the first pulse in the prompt emission; Lü et al. 2017), needs to be introjected. The data analysis of GRB 190109A prompt emission suggests distinct thermal emissions in all the time-resolved spectra of GRB190109A throughout the whole burst prompt emission from Pulse I to Pulse IV. Furthermore, the late X-ray afterglows are in accordance with the standard external shock model.

The BB luminosity of the photospheric emission can be described as $L = 16\pi R^2(1+z)^4\sigma T^4/\Gamma^2$, where R is the photospheric radius, σ is the magnetization degree, and Γ is the Lorentz

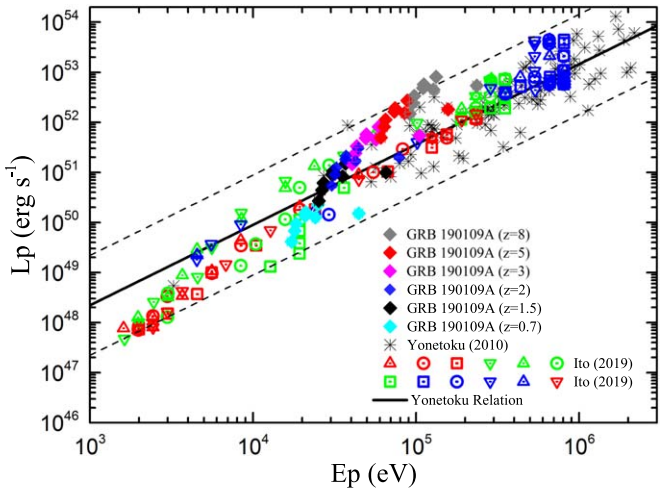

Figure 8. The relation of spectral peak energy E_p and peak luminosity L_p (*Yonetoku* relation). Two dashed lines located below and above the best-fit curve show the 3σ systematic error regions of the *Yonetoku* relation. Assuming the redshifts $z = 0.7$ (cyan diamond), 1.5 (black diamond), 2.0 (blue diamond), 3.0 (magenta diamond), 5.0 (red diamond), and 8.0 (gray diamond), the results of GRB 190109A time-resolved spectra are consistent with those of Yonetoku et al. (2010) and photospheric emission simulation results (Ito et al. 2019).

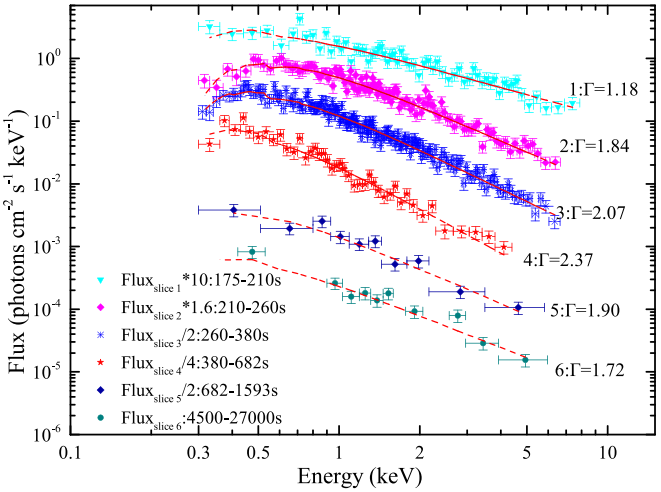

Figure 9. Spectral energy distribution analysis of GRB 190109A X-ray emission in six selected time intervals. They can be well fitted with a single PL function. The dashed lines show the intrinsic PL spectra derived from the joint fits. The photon indices are also marked.

Table 3
Spectral Analysis of the X-Ray Afterglows in Selected Time Intervals

Interval(s)	Model(PGSTAT/dof)	PhoIndex(Γ)
175−210	PL(65.07/58 = 1.12)	1.18 ± 0.06
210−260	PL(105.44/107 = 0.99)	1.84 ± 0.13
260−380	PL(170.92/168 = 1.02)	2.07 ± 0.04
380−682	PL(47.27/39 = 1.21)	2.37 ± 0.11
682−1593	PL(9.87/7 = 1.41)	1.90 ± 0.19
4500−27,000	PL(25.32/13 = 1.95)	1.72 ± 0.16

factor (e.g., Gao & Zhang 2015; Hou et al. 2018). The flux F is sensitive to the temperature with the proportion $F \propto T^4$. Generally, a higher flux corresponds to a higher-temperature BB component in the photosphere model (e.g., Golenetskii et al. 1983; Kargatis et al. 1994; Borgonovo & Ryde 2001; Fan et al. 2012). As shown in Figure 7, the $kT-F$ can be well described with a broken PL function having the slope $\alpha_{kT-F,1} = 3.33 \pm 0.76$ (Pulses II–IV) and $\alpha_{kT-F,2} = -0.40$ (Pulse I), which prominently deviates from the relationship of Pulses II–IV. To compare with the other previously reported thermal-dominated GRBs (GRB 081221, GRB 090902B, GRB 100507, GRB 101219B, and GRB 160625B), we redo the data reduction to get the kT and F. As shown in Figure 10, the positive-monotonic relations of $F \propto kT$ are obtained for all GRBs, e.g., $F \propto kT^{2.57\pm0.43}$ (GRB 081221), $F \propto kT^{2.25\pm0.16}$ (GRB 090902B), $F \propto kT^{1.42\pm0.69}$ (GRB 100507), $F \propto kT^{2.43\pm0.27}$ (GRB 101219B), and $F \propto kT^{4.21\pm0.51}$ (the first pulse in GRB 160625B). Hou et al. (2018) suggested that the deviation of the observed dependence concerning the BB flux on temperature to the theoretical T^4 should be attributed to some mild temporal evolution of the photosphere radius and/or the Lorentz factor. Therefore, the $kT-F$ in Pulses II–IV is in keeping with photospheric emission prediction and the previous results (e.g., Fan et al. 2012). However, Pulse I of GRB 190109A markedly deviates from the relationship of Pulses II–IV, with a negative-monotonic relation $F \propto kT^{\alpha_{kT-F,2}} = kT^{-0.40}$. Such a deviation implies that the origin of Pulse I BB spectra may have different physical processes from Pulses II–IV.

The deviation of the $kT-F$ correlation occurs in the early stage, which may be related to a different physical process. A cocoon component can be produced when the jet breaks through the stellar envelope of the progenitor star (e.g., Woosley 1993; MacFadyen & Woosley 1999; Ramirez-Ruiz et al. 2002; Lazzati & Begelman 2010; Nakar & Piran 2017). In previous work, a cocoon component is invoked as an explanation for the thermal emission of GRBs (Ghisellini et al. 2007; Piro et al. 2014) or for the precursor of GRBs (Lü et al. 2017) and the early X-ray afterglow of GRBs (Ramirez-Ruiz et al. 2002; Pe'er et al. 2006; Lazzati et al. 2010; Piro et al. 2014; Nakar & Piran 2017; Valan et al. 2018). Nakar & Sari (2012) also suggested that the early γ-ray emission may be produced by a (mildly) relativistic shock breakout as the cocoon's forward shock emerges from the stellar envelope, and the later γ-ray may be produced by the jet if a relativistic jet can be launched successfully. Ioka et al. (2019) proposed that the expected thermal temperature evolution as a function of the radiation energy flux in the shock breaking out from a stellar wind could be a negative relation. Besides, while BB spectra are produced by the cocoon material or the photosphere of the matter-dominated jet since the physical process differs, the appreciable deviations from the standard fireball are thus prone to happen (Ramirez-Ruiz et al. 2002). The relation of $kT-F$ in the early phase (Pulse I) of GRB 190109A deviates apparently from that in the late phase (Pulses II–IV), suggesting that the origin of BB spectra from the early phase (Pulse I, $F \propto kT^{-0.40}$) to the late phase (Pulses II–IV, $F \propto kT^{3.33\pm0.76}$) may be the transition from a cocoon surrounded by a jet to the photosphere of the matter-dominated long-duration jet.

4.2. BB+PL Model?

As is mentioned in Sections 3.1 and 3.2, it is hard to distinguish which one is better between the BB model and the BB+PL model merely from the results of BIC. For the typical GRB 090902B, the nonthermal component PL extended up to the high-energy GeV band, possibly resulting from the contributions of synchrotron emission, inverse Compton, or

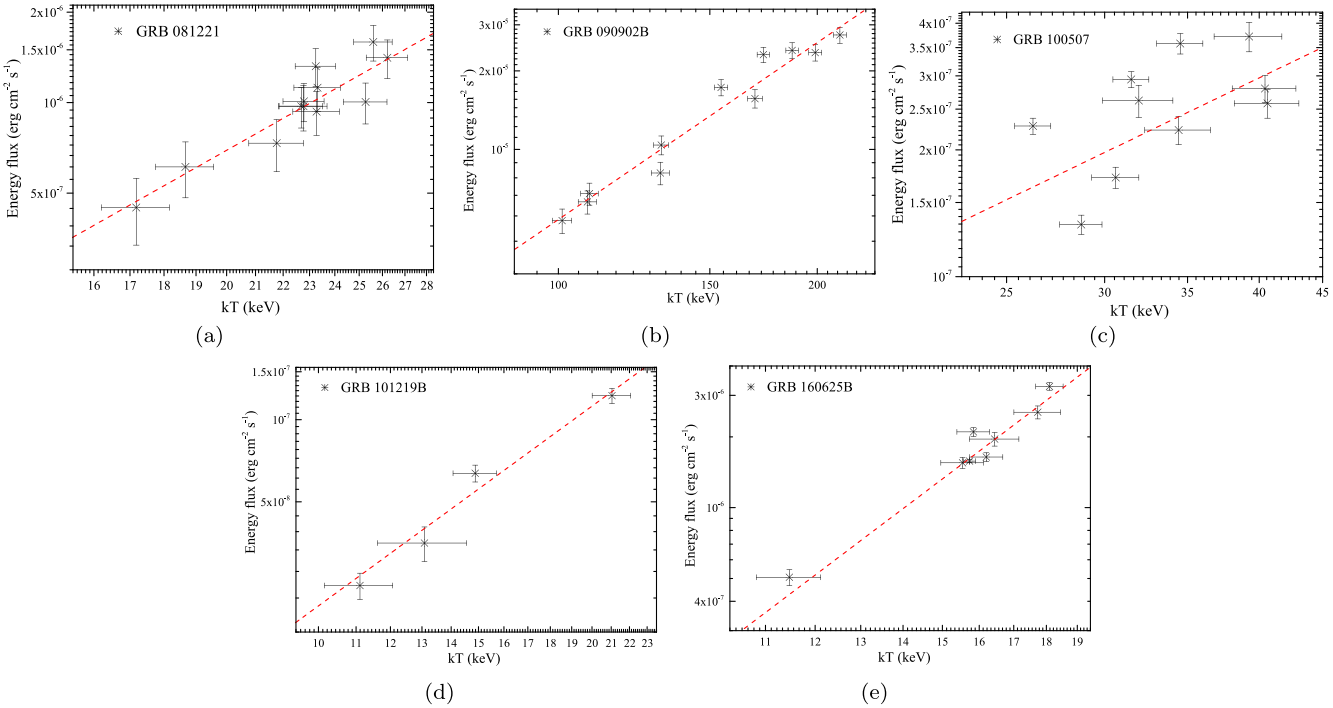

Figure 10. Temperature vs. energy flux of the BB for the time-resolved spectra of GRB 081221, GRB 090902B, GRB 100507, GRB 101219B, and GRB 160625B. (a) The relation of GRB 081221 is $F \propto kT^{2.57\pm0.43}$; (b) the relation of GRB 090902B is $F \propto kT^{2.25\pm0.16}$; (c) the relation of GRB 100507 is $F \propto kT^{1.42\pm0.69}$; (d) the relation of GRB 101219B is $F \propto kT^{2.43\pm0.27}$; (e) the relation of GRB 160625B is $F \propto kT^{4.21\pm0.51}$ (the first pulse in GRB 160625B).

Comptonization of the thermal photons by energetic electrons originating after dissipation of the kinetic energy above the photosphere (e.g., Pe'Er et al. 2012). The BB temperatures of GRB 190109A vary from 8.2 to 24.7 keV, which are much lower than for GRB 090902B.

Furthermore, the spectrum in the Swift/XRT band is well depicted by a PL function. Notably, the prompt phase (time slice 1, as shown in Figures 2 and 9) smoothly connects to Swift/BAT data, having a harder photon index $\Gamma = -1.18 \pm 0.06$. There may be a superposition of thermal and nonthermal components in the prompt emission. The inverse Compton scattering may produce a PL tail that extends from the peak of the thermal radiation, at several hundred keV, to several tens of MeV, and possibly up to GeV energies (e.g., Lazzati & Begelman 2010). However, there is no detection prompt emission data from Swift/BAT in the time window of slice 1, which can verify this speculation.

4.3. Estimated Photosphere Parameters

The jet compositions of GRBs are suggested to be diverse (e.g., Zhang & Yan 2011; Gao & Zhang 2015). The observed temperature and flux of the BB, together with the radius of the jet base (size of the central engine) r_0 and the assumed z, can give us useful information about the physical parameters of the photosphere (e.g., Pe'er et al. 2007; Gao & Zhang 2015). Following Gao & Zhang (2015), we calculate the photosphere parameters, e.g., the radius of the photosphere $r_{\rm ph}$, the Lorentz factor of the photosphere $\Gamma_{\rm ph}$, the magnetization parameter at the photosphere $\sigma_{\rm ph}$, the magnetization at the central engine σ_0, the dimensionless entropy of the hot fireball component η, and the magnetization parameter at$\sim 10^{15}$ cm σ_{15}. In the calculations we assume that there is no dissipation below the photosphere. The redshifts z are assumed to be from 0.7 to 8. The radii of the jet base are assumed to have the initial conditions for $r_0 = 10^7$ cm. The calculation of the photosphere parameter for GRB 190109A based on BB model fitting results is shown in Figure 11. The radius of the photosphere $r_{\rm ph}$ varies from 1×10^{11} cm to 2×10^{12} cm. The Lorentz factor of the photosphere $\Gamma_{\rm ph}$ varies from 50 to 500. We also presented the calculation of the photosphere parameter for GRB 190109A based on BB+PL model fitting results (as shown in Figure 12). The value of magnetization at the central engine is $\sigma_0 \ll 1$, the value of dimensionless η ranges from 200 to 5000, the value of radius of the photosphere $r_{\rm ph}$ ranges from 1×10^{11} cm to 2×10^{12} cm, the value of the Lorentz factor of the photosphere $\Gamma_{\rm ph}$ ranges from 40 to 500, and the value of the magnetization parameter at the photosphere $\sigma_{\rm ph}$ and at $\sim 10^{15}$ cm σ_{15} is still very small.

5. Summaries

The long GRB 190109A was detected by Fermi/GBM, Swift/BAT, and Swift/XRT, with a duration $T_{90} = 120$ s. It has four pulses: Pulse I (-4 to 20 s), Pulse II (20$-$50 s), Pulse III (50$-$90 s), and Pulse IV (90$-$120 s). The prompt emission of GRB 190109A is weak, and most of the photons were detected by the NaI detector in the Fermi/GBM. Almost no photons were detected by the BGO detector, and they were not detected by the Fermi/LAT. After performing a systematic analysis of GRB 190109A, we find the following interesting results:

1. We perform both the time-integrated and time-resolved spectral analyses concerning the prompt emission of GRB 190109A. Distinct thermal emissions in all the time-resolved spectra throughout four pulses in the whole burst prompt emission are found. Besides, the BB temperature kT varies from 24.7 to 8.2 keV for Pulse I to Pulse IV.

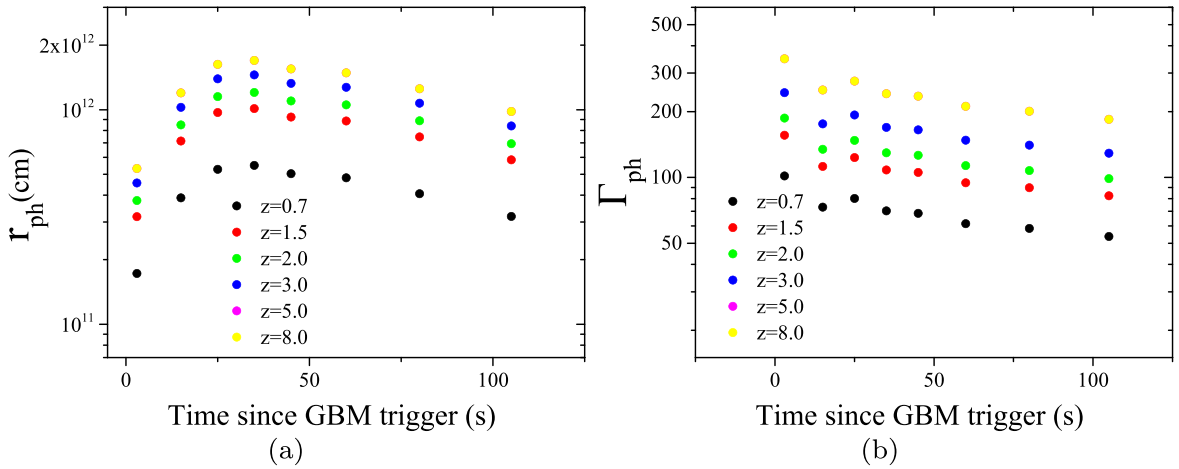

Figure 11. The calculation of the photosphere parameter for GRB 190109A based on BB model fitting results, assuming the size of the engine $r_0 \sim 10^7$ cm and redshift $z \sim 0.7$–8. (a) The radius of the photosphere $r_{\rm ph}$ varies from 1×10^{11} to 2×10^{12}; (b) the Lorentz factor of the photosphere $\Gamma_{\rm ph}$ varies from 50 to 500.

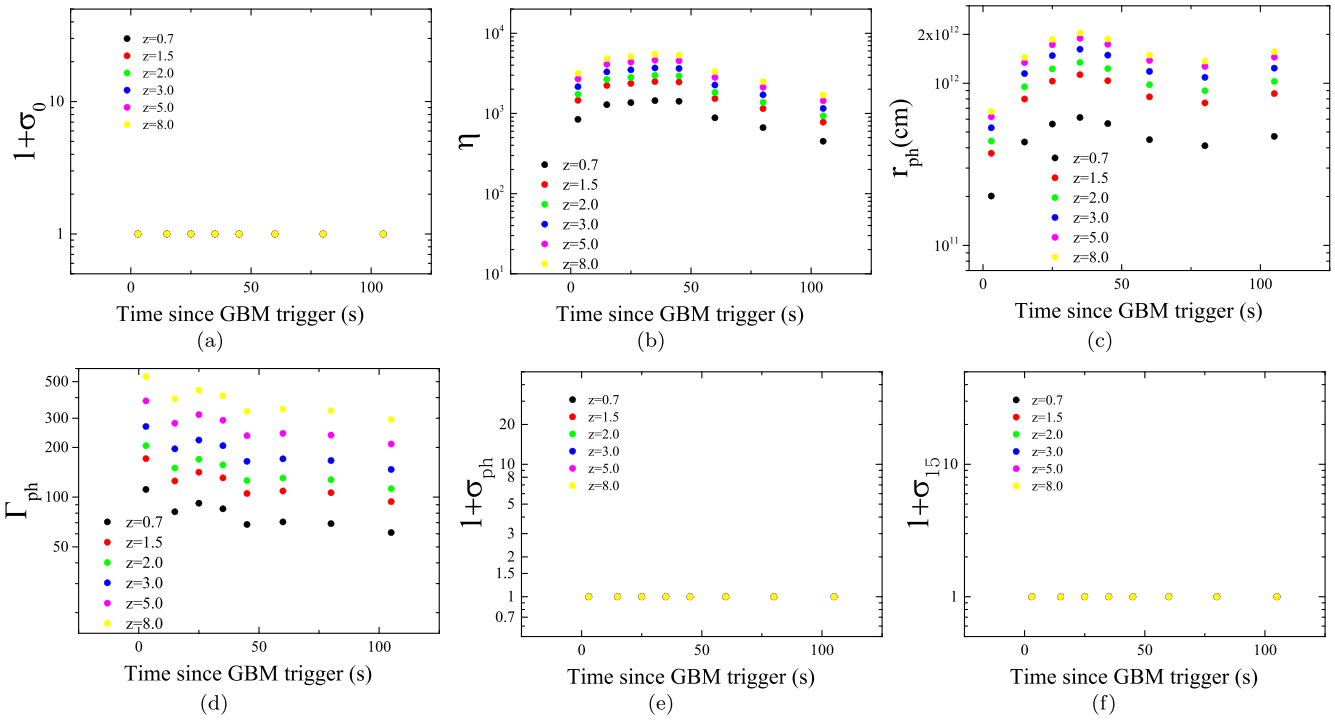

Figure 12. The calculation of the photosphere parameter for GRB 190109A based on BB+PL model fitting results, assuming the size of the engine $r_0 \sim 10^7$ cm and redshift $z \sim 0.7 \sim 8$. (a) The magnetization at the central engine σ_0; (b) the dimensionless η, with values ranging from 200 to 5000; (c) the radius of the photosphere $r_{\rm ph}$, with values ranging from 10^{11} to 10^{12}; (d) the Lorentz factor of the photosphere $\Gamma_{\rm ph}$, with values ranging from 40 to 500; (e) the magnetization parameter at the photosphere $\sigma_{\rm ph}$; (f) the magnetization parameter at $\sim 10^{15}$ cm σ_{15}.

2. A jet break is found in the late X-ray afterglow, which is consistent with the standard external shock afterglow model in the circumburst medium ISM.
3. The $kT-F$ relation is obtained with a positive-monotonic relation $F \propto kT^{\alpha_{kT-F,1}} = kT^{3.33\pm0.76}$ for Pulses II–IV (20−120 s) and negative-monotonic relation $F \propto kT^{\alpha_{kT-F,2}} = kT^{-0.40}$ for Pulse I (−4 to 20 s). Assuming $z = 0.7-8$, the $E_p-L_{\gamma,\rm iso}$ relation (*Yonetoku* relation) for the time-resolved spectra of GRB 190109A is in keeping with that for the time-integrated spectra of the *Yonetoku* sample (101 bursts; Yonetoku et al. 2010) and photospheric emission simulation results (Ito et al. 2019).

The relation of $kT-F$ in the early phase (Pulse I) of GRB 190109A deviates prominently from that in the late phase (Pulses II–Pulse IV), signifying the origin of BB spectra from the early phase (Pulse I) to the late phase (Pulses II–IV). In other words, the BB spectral origin of the early phase (Pulse I) may have different physical processes from that of the late phase (Pulses II–IV), which may be the transition from the cocoon surrounded by a jet to the photosphere of the matter-dominated jet.

Assuming that the size of the engine is around $r_0 \sim 10^7$ cm and redshift z from 0.7 to 8, we derive photosphere parameters for the BB model with the photosphere radius $r_{\rm ph} \sim 1 \times 10^{11}$ cm

to 2×10^{12} cm and the bulk Lorentz factor of the photosphere $\Gamma_{\rm ph} \sim 50-500$. However, relying simply on BIC results, one could hardly distinguish between the BB model and the BB+PL model to find the better one. Besides, detection data points around 700 keV may signify another component in the higher-energy zone. We also derive photosphere parameters for the BB +PL model, with the value of magnetization at the central engine being $\sigma_0 \ll 1$; the value of dimensionless η ranges from 200 to 5000; the value of radius of the photosphere $r_{\rm ph}$ ranges from 1×10^{11} cm to 2×10^{12} cm; the value of the Lorentz factor of the photosphere $\Gamma_{\rm ph}$ ranges from 40 to 500; and the value of the magnetization parameter at the photosphere $\sigma_{\rm ph}$ and at $\sim 10^{15}$ cm σ_{15} is still very small.

We thank the anonymous referee for suggestions that improved this paper. This work is supported by the National Natural Science Foundation of China (grant Nos. U1938201, 12133003, 11673006, 11533003), the Guangxi Science Foundation (grant Nos. AD17129006, 2016GXNSFFA380006, 2017GXNSFBA198206, 2017AD22006, 2018GXNSFGA 281007), the One-Hundred-Talents Program of Guangxi colleges, and High level innovation team and outstanding scholar program in Guangxi colleges. We also acknowledge the use of public data from the Swift and Fermi data archives.

ORCID iDs

Xiang-Gao Wang https://orcid.org/0000-0001-8411-8011
Da-Bin Lin https://orcid.org/0000-0003-1474-293X
En-Wei Liang https://orcid.org/0000-0002-7044-733X

References

Abbott, B. P., Abbott, R., Abbott, T. D., et al. 2017, ApJL, 848, L13
Arimoto, M., Asano, K., Ohno, M., et al. 2016, ApJ, 833, 139
Axelsson, M., Baldini, L., Barbiellini, G., et al. 2012, ApJL, 757, L31
Band, D., Matteson, J., Ford, L., et al. 1993, ApJ, 413, 281
Belkin, S., Klunko, E., Pozanenko, A., Mazaeva, E., & Volnova, A. 2019, GCN, 23654, 1
Beloborodov, A. M. 2010, MNRAS, 407, 1033
Berger, E., Price, P. A., Cenko, S. B., et al. 2005, Natur, 438, 988
Borgonovo, L., & Ryde, F. 2001, ApJ, 548, 770
Bromberg, O., Nakar, E., Piran, T., & Sari, R. 2011, ApJ, 740, 100
Daigne, F., & Mochkovitch, R. 2002, MNRAS, 336, 1271
Eichler, D., Livio, M., Piran, T., & Schramm, D. N. 1989, Natur, 340, 126
Yonetoku, D., Murakami, T., Tsutsui, R., et al. 2010, PASJ, 62, 1495
Fan, Y.-Z., Wei, D.-M., Zhang, F.-W., & Zhang, B.-B. 2012, ApJL, 755, L6
Fruchter, A. S., Levan, A. J., Strolger, L., et al. 2006, Natur, 441, 463
Gao, H., Lei, W.-H., Zou, Y.-C., Wu, X.-F., & Zhang, B. 2013, NewAR, 57, 141
Gao, H., & Zhang, B. 2015, ApJ, 801, 103
Ghirlanda, G., Pescalli, A., & Ghisellini, G. 2013, MNRAS, 432, 3237
Ghisellini, G., Ghirlanda, G., & Tavecchio, F. 2007, MNRAS, 375, L36
Giannios, D. 2008, A&A, 480, 305
Golenetskii, S. V., Mazets, E. P., Aptekar, R. L., & Ilinskii, V. N. 1983, Natur, 306, 451
Gropp, J. D., Barthelmy, S. D., Moss, M. J., Palmer, D. M., & Tohuvavohu, A. 2019, GCN, 23642, 1
Guiriec, S., Connaughton, V., Briggs, M. S., et al. 2011, ApJL, 727, L33
Guiriec, S., Daigne, F., Hascoët, R., et al. 2013, ApJ, 770, 32
Hou, S.-J., Zhang, B.-B., Meng, Y.-Z., et al. 2018, ApJ, 866, 13
Ioka, K., Levinson, A., & Nakar, E. 2019, MNRAS, 484, 3502
Ito, H., Matsumoto, J., Nagataki, S., et al. 2019, NatCo, 10, 1504
Kargatis, V. E., Liang, E. P., Hurley, K. C., et al. 1994, ApJ, 422, 260
Kass, R. E., & Raftery, A. E. 1995, J. Am. Stat.Assoc., 90, 773
Kouveliotou, C., Meegan, C. A., Fishman, G. J., et al. 1993, ApJL, 413, L101
Kumar, P., & Zhang, B. 2015, PhR, 561, 1
Larsson, J., Racusin, J. L., & Burgess, J. M. 2015, ApJL, 800, L34
Lazzati, D., & Begelman, M. C. 2005, ApJ, 629, 903
Lazzati, D., & Begelman, M. C. 2010, ApJ, 725, 1137
Lazzati, D., Morsony, B. J., & Begelman, M. C. 2010, ApJ, 717, 239
Lü, H.-J., Lü, J., Zhong, S.-Q., et al. 2017, ApJ, 849, 71
MacFadyen, A. I., & Woosley, S. E. 1999, ApJ, 524, 262
Matzner, C. D. 2003, MNRAS, 345, 575
Meegan, C., Lichti, G., Bhat, P. N., et al. 2009, ApJ, 702, 791
Mészáros, P., & Rees, M. J. 1997, ApJ, 476, 232
Mészáros, P., & Rees, M. J. 2000, ApJ, 530, 292
Nakar, E., & Piran, T. 2017, ApJ, 834, 28
Nakar, E., & Sari, R. 2012, ApJ, 747, 88
Narayan, R., Paczynski, B., & Piran, T. 1992, ApJL, 395, L83
Nava, L., Ghirlanda, G., Ghisellini, G., & Celotti, A. 2011, A&A, 530, A21
Oeda, M., Adachi, R., Murata, K. L., et al. 2019, GCN, 23649, 1
Paczynski, B. 1986, ApJL, 308, L43
Paczynski, B. 1991, AcA, 41, 257
Pe'er, A., Mészáros, P., & Rees, M. J. 2006, ApJ, 642, 995
Pe'er, A., Ryde, F., Wijers, R. A. M. J., Mészáros, P., & Rees, M. J. 2007, ApJL, 664, L1
Pe'Er, A., Zhang, B.-B., Ryde, F., et al. 2012, MNRAS, 420, 468
Piran, T. 1999, PhR, 314, 575
Piro, L., Troja, E., Gendre, B., et al. 2014, ApJL, 790, L15
Preece, R. D., Briggs, M. S., Mallozzi, R. S., et al. 1998, ApJL, 506, L23
Preece, R. D., Briggs, M. S., Mallozzi, R. S., et al. 2000, ApJS, 126, 19
Qin, Y., Liang, E.-W., Liang, Y.-F., et al. 2013, ApJ, 763, 15
Ramirez-Ruiz, E., Celotti, A., & Rees, M. J. 2002, MNRAS, 337, 1349
Rees, M. J., & Mészáros, P. 2005, ApJ, 628, 847
Ryde, F. 2005, ApJL, 625, L95
Ryde, F., Axelsson, M., Zhang, B. B., et al. 2010, ApJL, 709, L172
Ryde, F., & Pe'er, A. 2009, ApJ, 702, 1211
Sari, R., Piran, T., & Narayan, R. 1998, ApJL, 497, L17
Tanvir, N. R., Chapman, R., Levan, A. J., & Priddey, R. S. 2005, Natur, 438, 991
Thompson, C. 1994, MNRAS, 270, 480
Toma, K., Wu, X. F., & Mészáros, P. 2011, MNRAS, 415, 1663
Trotta, R. 2008, ConPh, 49, 71
Uhm, Z. L., & Zhang, B. 2014, NatPh, 10, 351
Usov, V. V. 1992, Natur, 357, 472
Valan, V., Larsson, J., & Ahlgren, B. 2018, MNRAS, 474, 2401
von Kienlin, A. 2019, GCN, 23658, 1
Wang, X.-G., Zhang, B., Liang, E.-W., et al. 2015, ApJS, 219, 9
Woosley, S. E. 1993, ApJ, 405, 273
Zhang, B. 2006, Natur, 444, 1010
Zhang, B. 2018, The Physics of Gamma-Ray Bursts by Bing Zhang (Cambridge: Cambridge Univ. Press)
Zhang, B., Fan, Y. Z., Dyks, J., et al. 2006, ApJ, 642, 354
Zhang, B., Lu, R.-J., Liang, E.-W., & Wu, X.-F. 2012, ApJL, 758, L34
Zhang, B., & Mészáros, P. 2002, ApJ, 581, 1236
Zhang, B., & Yan, H. 2011, ApJ, 726, 90
Zhang, B., Zhang, B.-B., Virgili, F. J., et al. 2009, ApJ, 703, 1696
Zhang, B.-B., Uhm, Z. L., Connaughton, V., Briggs, M. S., & Zhang, B. 2016, ApJ, 816, 72
Zhang, B. B., Zhang, B., Castro-Tirado, A. J., et al. 2018, NatAs, 2, 69